PCCP

RSC Publishing

PAPER

View Article Online
View Journal | View Issue

Cite this: *Phys. Chem. Chem. Phys.*, 2013, **15**, 6355

Small-angle water reorientations in KOH doped hexagonal ice and clathrate hydrates

H. Nelson,[a] S. Schildmann,[a] A. Nowaczyk,[a] C. Gainaru,[a] B. Geil[b] and R. Böhmer[a]

Received 11th January 2013,
Accepted 25th February 2013

DOI: 10.1039/c3cp00139c

www.rsc.org/pccp

Using deuteron nuclear magnetic resonance and dielectric spectroscopy KOH doped tetrahydrofuran clathrate hydrates and KOH doped hexagonal ice are studied at temperatures above 60 and 72 K, respectively. Below these temperatures proton order is established on the lattice formed by the water molecules. In the clathrate hydrate a new type of small-angle motion is discovered using deuteron spin–spin relaxation, line-shape analysis, and stimulated-echo experiments. Based on the latter results a model is developed for the local proton motion that could successfully be tested using random-walk simulations. It is argued that the newly identified small-angle motion, obviously absent in undoped samples, is an important feature of the mechanism which accompanies the establishment of proton order not only in doped clathrate hydrates but also in doped hexagonal ice. Specific motions of OH^- defects are demonstrated to explain the experimentally observed behavior. The relative importance of localized *versus* delocalized OH^- defect motions is discussed.

I. Introduction

There are probably no single-component substances for which more thermodynamic phases are known than for ice[1] with phase number XV discovered just a few years ago.[2] But why, after the identification of the ices named II and III in the year 1900, has this taken so long? Obviously, there is no simple thermodynamic path to all of these ice phases, many of which are not only (doubly) metastable,[3] but also require a sufficiently fast kinetics so that the transition can occur on accessible time scales. It has been debated whether or not intervals of up to 10 000 years are enough to allow for a transformation from the abundant hexagonal ice I_h to its proton-ordered companion phase XI in Antarctica[4] or elsewhere in our solar system.[5]

On laboratory time scales ice XI can be produced from ice I_h by doping with minute amounts of KOH and suitable thermal treatment at temperatures near 72 K.[6,7] An analogous phase transition was reported to occur for a KOH doped tetrahydrofuran (THF) clathrate hydrate near 60 K.[8,9] This cubic structure II (sII) clathrate can be considered as a model system since it comprises the same basic structural motif as ice I_h.[10] Due to the inclusion of guest molecules such as THF, the clathrate hydrate lattice is on average $\sim$30% less dense than that of ice I_h and upon KOH doping it exhibits proton order near about 60 K. With the local bonding geometry of its hydrate lattice similar to that of ice, it is no surprise that the transition into the ordered clathrate or ice structures takes place at relatively similar temperatures. But in spite of considerable experimental effort only incomplete proton order could be achieved, in ice[11,12] and in clathrates.[8,13]

In hydroxyl doped ice as well as in doped clathrate hydrates ionic and orientational defects are generated that cause a local breakdown of the Bernal–Fowler ice rules. The propagation of these defects activates protonic motion in large parts of the ice or hydrate lattice so that below the phase transition temperature proton order can emerge.[14,15] Due to the limited amount of KOH that can be incorporated into the hexagonal ice or into the cubic clathrate lattice during crystal growth, this activation or acceleration process does barely encompass the entire crystal so that typically ten percent or more of the protons remain disordered down to the lowest temperatures. There is evidence that KOH accelerates the proton dynamics in clathrates by up to 10 decades at 70 K, which is similar to the corresponding motional speed-up induced by doping ice I_h.[11] However, overall the dynamics in the doped THF clathrate is significantly faster than in KOH doped ice.[11] This acceleration of the proton dynamics in the clathrate was ascribed to the formation of weak hydrogen bonds between the guest molecules and the hydrate lattice thereby generating additional partial Bjerrum defects on the latter.[16,17] The extrinsic ionic defects induce the order–disorder transition which is associated with a change from the cubic to an orthorhombic low-temperature phase in a

[a] *Fakultät für Physik, Technische Universität Dortmund, 44221 Dortmund, Germany*
[b] *Institut für Physikalische Chemie, Georg-August Universität Göttingen, 37077 Göttingen, Germany*

doped THF clathrate hydrate.[18] The coupling between guest and host molecules has been used to study the impact of the phase change on the guest motion in detail.[19] The role played by hydrogen bonds or other host–guest interactions to establish a specific low-temperature phase still needs to be better understood. In this context studies of guest-free clathrate hydrates could be beneficial. Such crystals are, however, unstable at positive pressure and so far were explored only *via* computer simulations.[20,21] Furthermore, it is interesting to point out that similar order–disorder phenomena were reported to occur for THF clathrates based on inorganic host lattices unable to form hydrogen bonds.[22]

Recently, it was demonstrated that compressed salt hydrates, like *e.g.*, $LiCl{\cdot}6H_2O$, can form "salty ice" which strongly resembles high-pressure polymorphs of ice, with some ions occupying interstitials while other ions residing on regular lattice sites. In particular, a distorted variant of ice VII could be produced, with the lattice distortions apparently inhibiting a proton ordered low temperature state.[23,24] The important role that crystal strains can play in the formation of ice phases was emphasized.[25]

More puzzling is the finding that the formation of some ice phases, like ice XIII from ice V or ice XV from ice VI, is promoted by sub-percent amounts of the proton donor HCl to the parent phase, while KOH is very ineffective in this respect although it speeds up the reorientational motions in, *e.g.*, ice V.[26] It has been conjectured that while the proton acceptor KOH "induces" the only known ferroelectric ice phase, ice XI, acids do facilitate the production of antiferroelectric ices.[7] Clearly, the mechanisms driving these phase transitions have remained elusive.[27]

For nominally undoped ice and/or clathrate hydrates, on the other hand, the nature of the defect-induced motion in the hydrate lattice is theoretically[28] and experimentally well established. On the experimental side ^{2}H NMR[29–33] and ^{17}O NMR[34,35] as well as neutron scattering[36] and anelastic relaxation studies[37] have yielded important insights. Basically, proton transfer processes coupled with large-angle quasi-tetrahedral reorientations of H_2O molecules were found to dominate the dynamics, at least down to temperatures of 200 K at which these motions take place on the time scale of seconds. With the goal to unravel the mechanisms which accompany the emergence of proton order in *doped* ice and clathrate phases and in continuation of earlier work,[13] we performed a series of additional deuteron NMR experiments.

II. Experimental details

The cooling rate can have a major impact on the amount of KOH that is incorporated into the hydrate lattice and thus on the number of point defects. Therefore, deuteron NMR measurements were performed for differently prepared clathrate samples. In a first set of experiments $THF{\cdot}17D_2O$ single crystals were grown from solutions doped with a mole fraction $x = 10^{-3}$ of KOH.[38] These samples were then finely powdered, sealed in glass tubes, and eventually transferred to the spectrometer always keeping their temperature below about 100 K as described previously.[13] These powders are subsequently referred to as slowly cooled samples. Another set of polycrystalline clathrates was produced by first sealing stoichiometric clathrate solutions $THF{\cdot}17D_2O$, doped with 10^{-3} mole fraction of KOH, in an NMR tube and subsequent quenching of this solution in liquid nitrogen. Hexagonal heavy ice doped with 10^{-2} mole fraction of KOH was also prepared by quenching this aqueous solution in liquid nitrogen. Like in previous work,[13] care was taken that after initial cool-down the samples were not heated to temperatures above 200 K in order to avoid (ionic) impurity atoms that are expelled from the crystal lattice.

The NMR measurements were carried out at deuteron Larmor frequencies of 46.46 MHz (slowly cooled clathrate samples) or 55.55 MHz (quenched clathrate and ice samples). Further details regarding our NMR measurements can be found elsewhere.[13,33]

III. Results and analyses

A. Spin-lattice relaxation of quenched and slowly cooled samples

Just below the melting point the deuteron spin-lattice relaxation time T_1 of KOH doped ice is barely distinguishable from that of its nominally pure counterpart, see Fig. 1, and the same is true for THF clathrate hydrates (not shown). For pure ice T_1 monotonically increases with decreasing temperature reaching relaxation times of about 10^4 s near 150 K (below this temperature data acquisition would become increasingly annoying).[29] Down to 200 K the KOH doped sample exhibits T_1 behavior similar to that of pure ice, but at lower temperatures T_1 tends to saturate at values well below 1000 s. Finally, upon cooling to below 150 K, the spin-lattice relaxation times of doped ice become significantly shorter.

A similar T_1 pattern is observed for THF clathrate hydrates. Here, as Fig. 1 also shows, spin-lattice relaxation is sped up by KOH doping for 100 K $< T <$ 200 K.[39] Below $\sim$100 K, T_1 is not

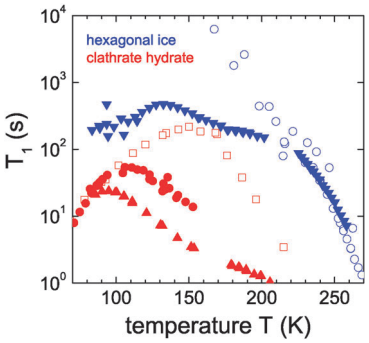

Fig. 1 Temperature dependent spin-lattice relaxation times of undoped hexagonal ice (open blue circles)[31] as well as of undoped THF clathrate hydrates (open red squares),[32] all measured at 55 MHz. The data are compared with those for doped samples from the present work: the downward blue triangles represent results for KOH doped ice recorded at a Larmor frequency of 55 MHz. The red filled circles and the red filled upward triangles correspond to the slowly cooled and the quenched doped clathrate hydrate, respectively. These latter two data sets were measured at 46 MHz.

affected by doping but rather by the reorientational slowing-down of the THF guests in their hydrate cages. The latter effect has often been studied in undoped clathrate samples and is well understood.[31,32,40,41] However, above about 100 K the temperature dependence of the T_1 relaxation is obviously dominated by KOH doping as well as by the thermal history of the sample. The T_1 times for the quenched, doped sample deviate most from those of the undoped clathrate (*e.g.*, by a factor of about 100 near 150 K). For the slowly cooled clathrate the corresponding effects are similar albeit slightly less pronounced. This indicates that for a given temperature, proton motion is fastest in the quenched and slowest in the undoped sample.

The spin-lattice relaxation times of the clathrate hydrates are always very much shorter than those of ice. This can be related to the formation of hydrogen bonds between the ether oxygen of the THF molecules with the protons of the hydrate lattice, which generate partial L-type Bjerrum defects. These defects facilitate protonic† motions rendering in turn also T_1 shorter. In the same vein, the quenched samples show further reduced T_1 times, as compared to the slowly cooled samples. This further reduction arises because slow crystal growth and annealing at temperatures above 200 K result in liberation of ionic impurities, *e.g.*, K^+, on the crystal surface which reduces the number of point defects in the interior of the crystal.[13,45] Conversely, quenched samples show a higher defect density which in turn accelerates the dynamics on the hydrate lattice and in the present case shortens T_1.

The very long deuteron spin-lattice relaxation characterizing ice I_h renders detailed studies of their dynamics enormously time consuming. This is why, in the following, we study the clathrate system much more thoroughly.

B. Slow dynamics induced by point defects

In KOH doped ice as well as in doped THF clathrate hydrates dielectric spectroscopy and/or calorimetric measurements have provided evidence for a relaxation process which is much faster than the one detected in undoped samples.[8,9,11] In Fig. 2 we summarize results concerning the THF clathrate hydrate from the literature.[8,9] For KOH doped ice we reproduce dielectric relaxation times,[11,42–45] mostly collected in the book of Petrenko and Whitworth,[1] and add a data set on D_2O ice doped with 10^{-2} mole fraction of KOH recorded in our laboratory. The latter time constants are included here to ensure comparability with the NMR data that will be discussed in the following sections.

Fig. 2 shows reorientational time constants of doped ice that were detected with dielectric spectroscopy in a range from about 10 μs to 10 s. In this time range stimulated-echo experiments are applicable, see Section III.B.1. For the doped clathrate hydrates, at a given temperature, also sub-microsecond and microsecond time scales are accessible. As detailed in

† More strictly, we should speak here of 'deuteronic' rather than of protonic motion. However, in the present article we use these terms as well as symbolic notations such as O–H···O and O–D···O interchangeably as long as they appear sufficiently unambiguous.

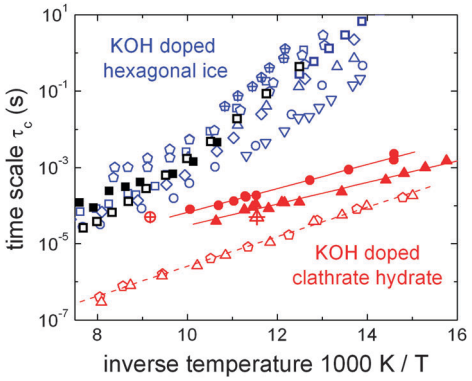

Fig. 2 Arrhenius plot of KOH doped hexagonal ice and of KOH doped THF clathrate hydrate samples. Dielectric relaxation times are marked by open symbols, NMR data by filled symbols. The dielectric data on ice were taken from ref. 42, see also ref. 1. Dielectric time constants on doped ice from this work (black open squares) are shown as well. The crossed pentagons represent time constants from friction/shear measurements on KOH doped hexagonal ice from ref. 37. The dielectric data on THF·17H_2O are from ref. 11 (triangles) and from ref. 9 (pentagons). The F_2 measurements from the present work are represented by black filled squares (hexagonal ice), by red filled circles (slowly cooled hydrate), and red filled upward triangles (quenched hydrate). If the time scale from T_2 measurements are assumed to be 50 μs, as shown here, for the KOH doped slowly cooled THF·17D_2O sample (red crossed circle) as well as for the quenched doped clathrate hydrate (red crossed triangle), then best agreement with the F_2 measurements is obtained. The solid lines represent an activation energy of (6.7 ± 0.5) kJ mol^{-1}. The dashed line corresponds to an activation energy of 7.4 kJ mol^{-1} as reported in ref. 9 and 11.

Section III.B.2, this allows us to explore the proton dynamics additionally *via* measurements of spin–spin relaxation and of line shape changes.

1. Detection *via* stimulated deuteron echoes. Stimulated echoes provide direct access to the reorientation of OD bonds because the quadrupole perturbed NMR frequency ω_Q depends on how the external magnetic field is oriented with respect to the principal axis system of the electrical field gradient (EFG) tensor at the deuteron site. More quantitatively

$$\omega_Q = \pm\frac{1}{2}\delta\left(3\cos^2\theta - 1 - \eta\sin^2\theta\cos^2\phi\right), \qquad (1)$$

with θ and ϕ describing the orientation of the OD bond in the usual fashion. The anisotropy parameter δ and the asymmetry parameter η are characteristics of the EFG tensor. Typical values for deuterons in OD bonds are $\delta = 3e^2qQ/(4\hbar) = 2\pi \times 162$ kHz and $\eta = 0.1$.[30,41]

Stimulated-echo spectroscopy enables one to acquire, *e.g.*, the two-time correlation function

$$F_2(t_p, t_m) = \langle\cos[\omega_Q(0)t_p]\cos[\omega_Q(t_m)t_p]\rangle, \qquad (2)$$

as a function of the so-called mixing time t_m during which the molecular dynamics can take place. The evolution time t_p appearing in eqn (2) is an experimentally adjustable parameter which sets the angular sensitivity of the experiment.[46] By explicitly varying t_p, details of the geometry of the molecular motion can be mapped out, as will be exploited in Section III.C, below. Keeping t_p fixed one can monitor the overall temperature dependence of the deuteron dynamics.

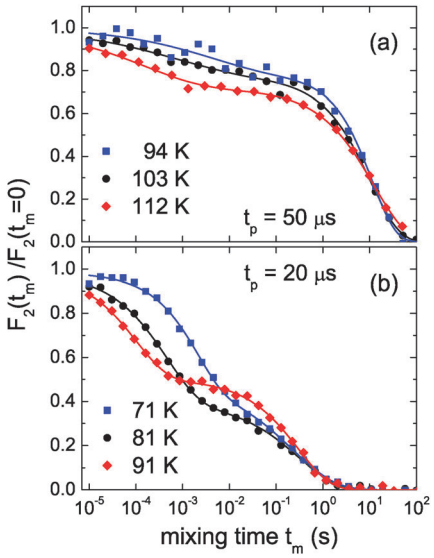

Fig. 3 Stimulated deuteron echo decays recorded (a) for rapidly cooled heavy ice I_h doped with a mole fraction of 10^{-2} KOH and (b) for quenched THF·17D_2O doped with a mole fraction of 10^{-3} KOH at various temperatures. The evolution times are indicated and the solid lines are fits using eqn (3).

Stimulated-echo data for doped ice and for doped clathrate hydrates are shown in Fig. 3(a) and (b), respectively. For both substances one recognizes a two-step decay with the faster process, unlike the slower one, showing a pronounced temperature dependence. After correction for spin-lattice relaxation, the measured correlation functions were fitted using

$$F_2(t_m) = \{(M_0 - M_1)\exp[-(t_m/\tau_f)^{\beta f}] + M_1\}\exp[-(t_m/\tau_s)^{\beta s}]. \quad (3)$$

Here the M_i denote various magnetization levels and $\tau_{f,s}$ and $\beta_{f,s}$ designate correlation times and stretching parameters, respectively, for the faster or for the slower process. Below about 100 K for the clathrate hydrate τ_s saturates near 0.5 s as already documented elsewhere,[13] see also Fig. 3(b). In Fig. 3(a) one recognizes that τ_s of doped ice is of the order of 10 s. Comparison with the results in Fig. 1 demonstrates for both substances that τ_s is much shorter than the respective T_1 times between 100 and 200 K.

For the doped clathrate hydrate τ_s was previously conjectured to be associated with a large-angle rotational motion[13] similar to the one known from undoped THF clathrates.[30] A similar motion is likely to cause the slow stimulated-echo decay in doped ice seen in Fig. 3(a), but in view of the very long spin-lattice relaxation times, which would necessitate enormously time consuming experiments, we refrain from checking this potential analogy more carefully.

For comparison with the dielectric relaxation times τ_D the shorter correlation times τ_f from NMR are also included in the Arrhenius plot, Fig. 2. For doped ice one observes very good agreement when comparing the results from the two experimental techniques. However, for the doped clathrate hydrate the situation is more complex. While the temperature dependences of the time constants from dielectric spectroscopy and from NMR show similar trends with temperature, for the quenched sample τ_f is a factor of about 6 larger than τ_D. Even more pronounced differences, *i.e.*, longer time constants, show up for the slowly cooled sample, analogous to the observations made in Fig. 1. To explore the origins of this difference in time scales for the doped clathrate hydrates we performed further experiments and numerical simulations as detailed in the following sections.

It should be noted that the proton ordering transition takes place over a range of several Kelvin and seems to depend on the thermal history of a sample: for the quenched hydrate sample the time constants τ_f, which were recorded upon cooling, extend to below the previously determined phase transition temperature of about 65 K.[13] In the present work, we find a transition temperature for rapidly cooled, KOH doped THF·17D_2O of $\approx$ 60 K.

When comparing the results from doped ice with those from the doped clathrate, *cf.* Fig. 3, it is striking that not only the time scales but also the amplitudes of the faster process differ vastly. With conventional dielectric spectroscopy and with NMR it is difficult to check to what extent the doped ice sample orders ferroelectrically. Although the defect-induced activation process will facilitate the establishment of local proton order, it cannot be ruled out that the presence of OH^- defects has activated a significantly smaller fraction of the hexagonal ice than the clathrate sample.

2. Detection *via* spectral line shapes and spin–spin relaxation. In Fig. 4 we compile a representative set of solid-echo spectra recorded for a slowly cooled clathrate hydrate. At first glance the spectra all look very similar, but a closer inspection reveals that the line shapes undergo small but significant changes as a

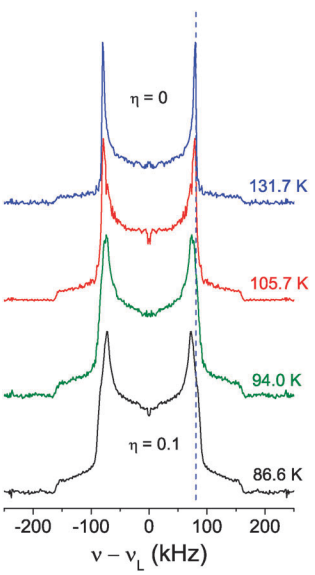

Fig. 4 Solid-echo spectra of KOH doped THF·17D_2O recorded with a refocusing delay of 20 μs and shifted vertically for clarity. At the lowest temperature the spectrum is characterized by an asymmetry parameter η = 0.1 while at the highest temperature η = 0. The vertical line highlights that change in line shape. One observes that the outer singularities are temperature independent, indicating that the anisotropy parameter $\delta = 2\pi \times 160$ kHz is constant.

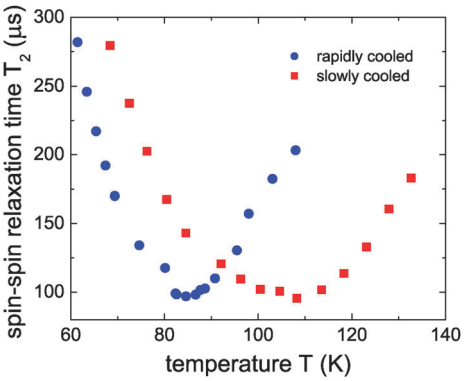

Fig. 5 Spin–spin relaxation times T_2 associated with the small-angle motion of quenched and slowly cooled KOH doped THF·17D_2O.

function of temperature. Below 100 K the powder pattern is that of a motionally rigid solid indicative of parameters in typical OD bonds (δ^{-1} = 1.0 μs and η = 0.1 for the spectrum at 87 K). For T larger than about 100 K, the outer edges of the spectral horns become more steep, as is typical for an axially symmetric EFG tensor (η = 0), while the anisotropy parameter δ remains essentially unaffected. This relatively minor change in the line shape is due to a motion which modulates the quadrupolar precession frequencies only moderately. In other words, the spectra indicate that the water molecules perform small-angle jumps.

Any line shape transition should be reflected in a minimum of the temperature dependent spin–spin relaxation time T_2. Indeed, Fig. 5 documents that using the solid-echo sequence such a minimum can be detected with a mean $T_{2,\min}$ = (96 ± 10) μs (at 109 K for the slowly cooled sample and at 87 K for the quenched one). This experimentally observed minimum T_2 is about 100 times longer than what is expected in the presence of *isotropic* molecular reorientations.[47] Thus, the large value of the minimal T_2 again demonstrates that highly restricted angular protonic motions characterize the dynamics in doped clathrate hydrates.

One can extract a time scale τ_J for that proton jump motion from the data shown in Fig. 5. At the temperature at which the minimum in the spin–spin relaxation time shows up the fluctuating part of the quadrupolar frequency $\Delta\omega_Q \equiv \sqrt{(\Delta\omega_Q)^2}$ equals τ_J^{-1}. In the framework of the Anderson–Weiss theory[48–50] such an equality has been derived for a number of situations,[51,52] and $\Delta\omega_Q\tau_J \approx 1$ also applies to anisotropic motions monitored *via* the solid-echo technique. In order to exploit this relationship quantitatively knowledge of $\Delta\omega_Q$ is required.

In a simplified fashion $\Delta\omega_Q$ as well as the angular fluctuations $\Delta\theta$ can be estimated from $T_{2,\min}$ as follows: since η is small, fluctuations in the azimuthal angle, $\Delta\phi$, affect $\Delta\omega_Q$ much less than fluctuations in $\Delta\theta$, *cf.* eqn (1), and will be neglected in the following. From the derivative of eqn (1) with respect to the polar angle one obtains $\Delta\omega_Q = -(3\delta/2)\ \Delta\theta\ \sin(2\theta)$. Here, $(3\delta/2)\Delta\theta$ can be interpreted as a reduced anisotropy parameter δ_{red}. Approximating the trigonometric functions in

$$\frac{\Delta\omega_Q}{\omega_Q} = \frac{-\sin 2\theta}{\frac{1}{2}(3\cos^2\theta - 1)}\frac{\delta_{red}}{\delta} = \frac{-\frac{3}{2}\delta\sin 2\theta}{\frac{1}{2}\delta(3\cos^2\theta - 1)}\Delta\theta, \qquad (4)$$

by unity one thus estimates $\Delta\omega_Q/\omega_Q \sim \delta_{red}/\delta \sim -\frac{3}{2}\Delta\theta$.

If $J(\omega)$ denotes the spectral density of an isotropic motional process and K is a constant of order 1 then, near the T_2 minimum (denoted $T_{2,iso}$), for the spin–spin relaxation one approximately has $1/T_2 \approx K\delta_Q^2 J(\omega_Q)$.[50] Similarly, for an anisotropic process one may write $1/\tilde{T}_2 \approx \tilde{K}\delta_{Q,red}^2\tilde{J}(\omega_Q)$ with the minimum spin–spin relaxation time like above denoted $T_{2,\min}$. Assuming that the relevant quadrupolar couplings and spectral densities are similar, *i.e.*, that $\tilde{K} \approx K$ and $\tilde{J} \approx J$, the ratio of the minimum spin–spin relaxation rates is

$$\frac{1/T_{2,\min}}{1/T_{2,iso}} \approx \frac{\delta_{red}^2}{\delta^2} \sim \left(-\frac{3}{2}\Delta\theta\right)^2. \qquad (5)$$

For an isotropic motional process $T_{2,iso}$ is of the order of $\sim(1\ \mu s)^{-1}$.[47] From our experiments (*cf.* Fig. 5) we find $T_{2,\min} \sim (96 \pm 10)$ μs so that $T_{2,iso}/T_{2,\min}$ is about 1/100. Based on eqn (5) the mean angular excursion is estimated to be $\left\langle\sqrt{(\Delta\theta)^2}\right\rangle \equiv \Delta\theta \sim \frac{2}{3}\sqrt{\frac{1}{100}} \sim 0.066$ which corresponds to an angle of $\sim 0.066 \times 180°/\pi \sim 4°$. In Section III.C.2 we will provide a more quantitative experimental determination of $\Delta\theta$ which essentially confirms the present estimate.

Combining $\Delta\omega_Q\tau_J \approx 1$ with the relation given just above [eqn (4)] one arrives at $1/\tau_J \approx |\Delta\omega_Q| \sim (3\delta/2)\,\Delta\theta\,\langle\sin(2\theta)\rangle$. Using $\langle\sin(2\theta)\rangle = \frac{1}{2}$, $\Delta\theta$ as just estimated, and δ^{-1} = 1.0 μs this yields $\tau_J \sim 20$ μs. Due to the crude assumptions leading to this result it should only be regarded as a best guess. Fig. 2 shows that $\tau_J \sim 50$ μs might be a better estimate because then good agreement is achieved with the correlation times measured using the stimulated-echo experiments for the slowly cooled *and* for the quenched sample.

C. Small-angle dynamics near the order–disorder transition

1. Deuteron echo experiments of clathrate hydrates. As pointed out in Section III.B.1 stimulated-echo experiments, when performed as a function of the evolution time t_p, are ideally suited to unravel details of motional geometries. In Fig. 3 we already provided data at constant evolution time t_p, indicating a two-step decay that could be fitted using eqn (3). As noted in Section III.B.1 the decay seen in Fig. 3 at longer times is presumably due to a large-angle jump process.

In Fig. 6 explicitly t_p dependent short-time decays are shown for a quenched, KOH doped clathrate hydrate sample that were recorded at 72.6 K and normalized using $\exp[-(t_m/\tau_s)^{\beta_s}]$, *cf.* eqn (3). From Fig. 6 one recognizes that the time scale on which the short-time decays take place is essentially independent of t_p. However, the plateau value appearing at long time, defined as the so called final-state amplitude, $Z = M_1/M_0$, decreases strongly with increasing evolution time.

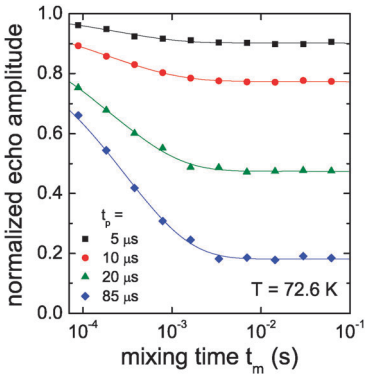

Fig. 6 Stimulated deuteron echo decays of a quenched THF·17D_2O sample doped with a mole fraction of 10^{-3} KOH. The data were normalized so that they solely reflect the short-time decay. The latter takes place on a time scale τ_f which is essentially independent of the evolution time t_p. The solid lines reflect a suitably adapted Kohlrausch function with a stretch exponent of $\beta = 0.56$.

Similar results were obtained at 75.1 K and at 70.1 K (not shown). All data were fitted using eqn (3) and yielded $\beta_s = 0.56 \pm 0.04$ and $\beta_f = 0.64 \pm 0.11$ as well as the parameters τ_s, τ_f, and Z as shown in Fig. 7(a). In the inset of this figure one recognizes that the experimentally determined time constants are practically independent of t_p except for small evolution times. The final-state amplitude reveals a more interesting behavior.

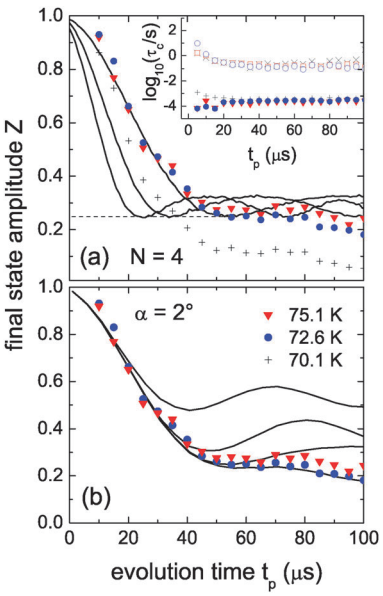

Fig. 7 Evolution time dependent final-state amplitudes $Z(t_p)$ derived from stimulated-echo experiments (symbols) and compared to random-walk simulations [lines, $Z^+(t_p)$] of the cone model described in Section III.C.2 and Appendix A. The solid lines are left shifted by 4 μs in order to account for the finite width of the radio-frequency pulses. From left to right the solid lines in frame (a) refer to cone opening half-angles of $\alpha = 4°$, 3°, and 2°. The dashed line highlights $Z = 1/4$ corresponding to $N = 4$ sites. In frame (b) the solid lines correspond to (from top to bottom) $N = 2$, 3, 4, and 6. The agreement of experimental data and simulation is excellent for $\alpha = 2°$ and $N = 6$. The inset in frame (a) shows the experimentally determined correlation times τ_c. Their t_p independence is in agreement with the results from the present random-walk simulations.

The $Z(t_p)$ values acquired at 75.1 K and at 72.6 K coincide within experimental error.

A puzzling observation can be made in Fig. 7(a) for T = 70.1 K. Here the entire $Z(t_p)$ pattern appears to be shifted downwards with Z reaching values much smaller than 1/6. As will become clear in Section III.C.2 none of our simulations can explain this observation. Of course if some impurity phase (like a proton ordered variant of the clathrate) would be present then this will affect the final state amplitude. However, all measurements presented in Fig. 7 were performed upon cooling, *i.e.*, a temperature below the order–disorder transition was never reached. Therefore, we can only speculate about the origin of the "shifted" $Z(t_p)$ pattern at 70.1 K. In this context we quote from Tajima *et al.* who note that "although the phase transition of ice I_h is of first order with a large discontinuity in the entropy, there is a premonitory effect above the transition temperature."[15] Presumably, similar arguments apply to the phase transition of the clathrate hydrate. So in the absence of a more satisfying explanation, in the following we will focus on the $Z(t_p)$ patterns recorded at the two higher temperatures.

It is well known[29,46,53] that the final-state amplitude $Z_\infty = Z(t_p \to \infty)$ is a measure of the number of magnetically inequivalent sites that an EFG tensor (*i.e.*, the corresponding OD bond axis) can reach in the course of a reorientation process if all the sites are equally populated. Experimentally Z_∞ is close to or below 0.25 (see the dashed line in Fig. 7) suggesting that four (or a few more) sites are involved in the jump process. It is also remarkable that Z_∞ is approached only for values of $t_p\delta \approx 50$. Such large values are indicative of small-angle motions.[53]

2. Jump geometry and its random-walk analysis. In ice and likewise also in clathrate hydrates large-angle jumps of the water molecules about their twofold axes are always accompanied by small-angle jumps, with both types of jumps occurring on the *same* time scale.[31] The inset in Fig. 7 clearly documents a separation of time scales for the small-angle and the large-angle jump by about 3 decades. This indicates that the small-angle process is different in nature than the jump motions previously identified, *e.g.*, in ref. 31.

In order to appreciate how a small-angle motion could come about, in Fig. 8(a) we illustrate a local structural building block of hexagonal ice. Here each oxygen atom is located in the center of a tetrahedron formed by its oxygen neighbors. Between the two oxygen atoms sketched in Fig. 8(b) a local mirror plane is present if one disregards the proton positions. Since in the solid the H–O–H angle α_{HOH} characterizing the water molecule differs somewhat from the tetrahedral angle of $\alpha_t \approx 109.5°$, the O–H···O bond is slightly nonlinear, *i.e.*, the O–H direction and the line connecting two adjacent O atoms enclose an angle of a few degrees.[31] Furthermore, this O–O line can be considered a local threefold axis, implying that the possible O–H directions can be thought to lie on the surface of a cone with an opening angle of 2α. To good approximation the semi-angle α of that cone is given by the difference $\alpha_t - \alpha_{HOH}$. Structural studies on ice I_h yielded $\alpha_{HOH} = (106.6 \pm 1.5)°$,[54,55] so that for hexagonal ice the semi-angle α is expected in the range from about 2° to 3°.

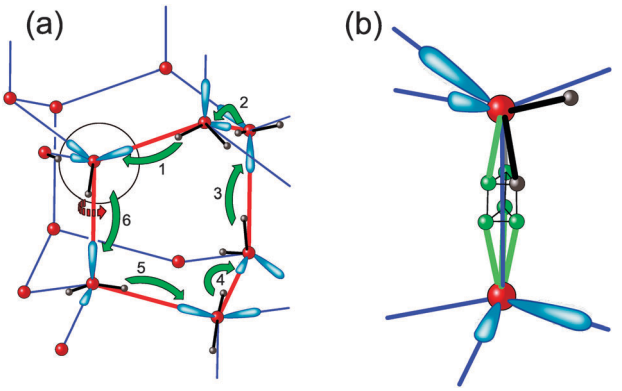

Fig. 8 (a) A local structural building block of hexagonal ice as represented by connected oxygen atoms (red spheres). Along a 6-ring, highlighted by the thick red lines, water molecules and an OH^- defect are sketched. The difference between the tetrahedral O–O–O bond angle and the slightly smaller H–O–H angle[10] leads to the existence of 6 distinguishable OH bond orientations at a given site. The numbered green arrows illustrate a sequence of local proton transfers which eventually result in a small-angle reorientation (indicated by a broken red arrow) on the encircled site. Frame (b) provides a schematic view of two adjacent, ''opposing cones'' between adjacent oxygen sites: each group of the three OH bonds can be thought to lie on the mantle of a cone with an opening angle of 2α. Between adjacent O sites we sketched the 6 orientations of the OH bonds compatible with the local symmetry.

The resulting opening angle 2α of $4\ldots6^\circ$ is compatible with the rough estimate for $\Delta\theta$ given in Section III.B.2 for the doped clathrate hydrate. In the clathrate hydrates the basic structural motif is the same as the one sketched in Fig. 8(b), but in the clathrates the angles enclosed by three adjacent oxygen atoms are somewhat distorted. Nevertheless, the mean O–O–O angle of 109.62° reported[10] for the THF clathrate is very close to α_t.

Now, we aim at conceiving a model that captures the essential geometrical aspects of the proton motion. It is clear that when the water molecules jump about the local three-fold axis just mentioned, the proton closer to the C_3 axis performs a cone-type of motion. In addition, a defect-induced proton transfer between sites on adjacent cones might occur. To check whether such a jump geometry is able to describe the experimental data quantitatively we performed random-walk simulations, see Appendix A. Such simulations were previously applied to various relaxation processes in disordered materials.[46,56–58]

In brief, stimulated-echo decay functions were generated from about 10^5 trajectories for different cone semi-angles α and for N equally populated sites. The transition rates among all sites were chosen to be identical. Then, the simulated $F_2(t_p,t_m)$ curves were fitted exactly as the experimental data. The fit parameters are presented in Fig. 7 as a function of the evolution time. As the inset shows, the time constants barely depend on the tested motional models and are essentially independent of t_p, at least for $t_p \geq 15$ μs. This insensitivity to t_p follows from our assumption of only a *single* jump rate. A more specific behavior is displayed by the final-state amplitude Z. Simulations for different cone angles 2α reveal that coincidence with the experimental data can be achieved when choosing α close to 2°, see Fig. 7(a) for $N = 4$.[59] Larger cone angles lead to a much more rapid decay of $Z(t_p)$ so that for $t_p \leq 40$ μs no agreement is possible. In a second step we kept α fixed and varied the number N of magnetically inequivalent sites. From Fig. 7(b) one infers that $N = 6$ yields the best agreement between simulation and experiment.

IV. Discussion

A. Motional models

The agreement between experiment and simulation that is documented in Fig. 7 is very convincing. But so far it was not discussed how the OH bonds can reach the 6 inequivalent orientations that are depicted in Fig. 8(b). A severe constraint of any motional model able to rationalize this geometrical feature is that it must not involve tetrahedral (*i.e.*, large-angle) reorientational jumps of water molecules because they are not observed experimentally on the time scale on which the small-angle jumps take place. Hence, we have to restrict our considerations to local Grotthus-like proton transfer mechanisms within a given hydrogen bond. Since the fast process (*cf.* Fig. 2) is only observed in KOH doped samples, it is natural to assume that OH^- defects play an important role.

A structural building block of hexagonal ice containing such a defect is sketched in Fig. 8(a). If we start with a regular, defect free configuration, which fulfills the Bernal–Fowler ice rules, and remove a proton, then a Bjerrum L defect [not shown in Fig. 8(a)] is simultaneously created. To reorient the proton attached to this OH^- group (designated proton p_1 in the following) two scenarios can be conceived.

• Scenario (a): only a single OH^- defect is the generator of a small-angle motion of this particular proton. Then, after a number of proton transfers, also in other hydrogen bridges, the OH^- defect has to return several times to its ''initial'' lattice site so that p_1 (more precisely the corresponding covalent OH bond) can eventually attain six different orientations.

• Scenario (b): the lattice site encircled in Fig. 8(a) is traversed by several different OH^- defects. This requires a sufficiently close spatial proximity of them, a situation that we will consider further below.

Let us first deal with the case that an OH^- defect goes in closed loops. An example for this type of concerted motion is sketched in Fig. 8(a). Here the proton configuration is constructed such that a cyclic passage of an OH^- defect is possible along the highlighted 6-ring. This passage requires the existence of a strict alternating lone-pair/proton sequence along the path. In Fig. 8(a) the numbered arrows indicate a possible sequence of Grotthus-like proton jumps. Now, it is important to realize that each proton transfer event from an adjacent proton-donating water molecule is associated with a small-angle rotation of the other proton of that molecule.

What else has happened when the OH^- defect has looped through a ring and eventually returned to its initial site? The protons on the participating 6-ring sites have all performed one transfer step in their almost linear O–H···O bonds and proton p_1 has additionally experienced a rotational jump, see the

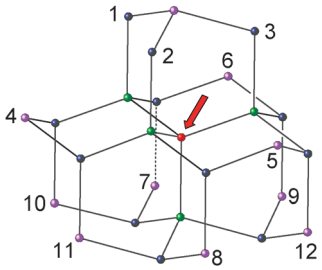

Fig. 9 Local structural motif of hexagonal ice with the dots representing oxygen atoms. The oxygen marked by the arrow (which is representative for all O atoms in the ice lattice) is connected to twelve 6-rings. These rings are numbered in an arbitrary order near the ''central'' oxygen site.

broken arrow in Fig. 8(a). The constraint that large-angle jumps should not be involved is also obeyed. Most importantly, the OH^- defect is not just back at its original position, but its orientation has changed. Furthermore, the lone-pair/proton sequence along the path has been inverted by this process. Consequently, the 6-ring highlighted in Fig. 8(a) is now blocked for another passage in the same direction of the considered OH^- defect.

Of course, the lattice site encircled in Fig. 8(a) belongs to several further 6-rings. As a sketch of the local structure of hexagonal ice shows, see Fig. 9, each lattice site is a member of twelve 6-rings. But not all of these rings can be entered by a given OH^- defect. It turns out that only half of them can be accessed and subsequently traversed in a cycle. This can be inferred from Fig. 10 which allows one to count the transition paths of an OH^- defect through a lattice site occupied by a water molecule. In principle, from each numbered position three paths lead through this site. However, the two lone pairs of the central water molecule prevent an OH^- defect from entering the corresponding pathways. Hence, six out of twelve passages are blocked and furthermore, a path *via* a lattice site conductive for an OH^- defect has to involve a proton at its entrance and a lone-pair at its exit.

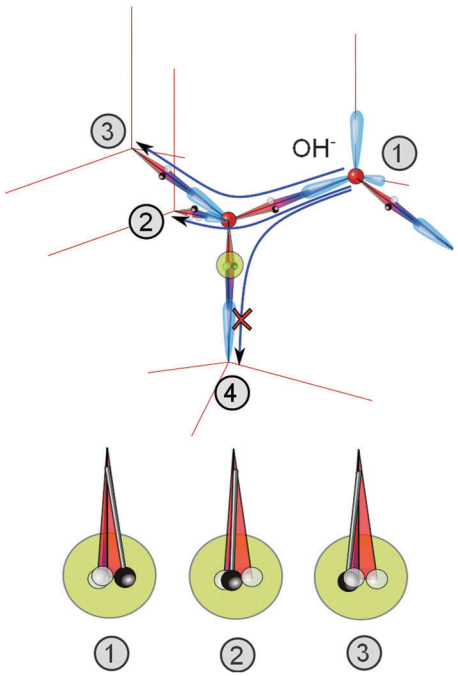

Fig. 10 Transition paths of an OH^- defect through a lattice site that is occupied by an H_2O molecule. The upper part of the figure shows that with the (arbitrarily) chosen orientation of the water molecule, the paths from site (1) to sites (2) and (3) are allowed while the pathway to site (4) is blocked, *i.e.*, not possible without violating the ice rules. The lower part of the figure shows the three possible orientations of the highlighted OH bond. Option (1) depicts the OH bond orientation that exists here prior to the passage of an OH^- defect. Options (2) and (3) occur if the defect moves to site (2) or to site (3), respectively. A Grotthus-type of proton transfer (not sketched in this figure) doubles the number of OH bonds to overall six orientations near the encircled site.

B. Passage probabilities for different scenarios

In the lower part of Fig. 10 we show examples for three final configurations of the proton p_1 compatible with the various pathways. Three more orientations can be accessed by this proton if one takes into account the mirror plane that locally exists between two adjacent oxygen atoms. If scenario (a) is considered, the question arises how likely it is that a given defect returns to its initial site. Semi-quantitative estimates are made in Appendix B. Basically, for short times we find that the return-to-origin probability is of the order of 10^{-3}. Since each defect has to return twice (*i.e.*, visit a site three times) to be at each site thrice, an elementary time step $\tau_e \sim 10^{-6}\tau_f$ has to be assumed. The consequences of this assumption are discussed further below.

For the passage of defects as sketched in Fig. 10(b) to (d) it is of course not necessary to assume that only a single OH^- is involved. The data in Fig. 7, *i.e.*, the finding that six distinguishable OH bond orientations are accessible at each lattice site, can be explained if each site is traversed by 3 *different* OH^- defects so that together with a Grotthus-like proton transfer six orientations are reached. The probability that a given lattice site is traversed by a defect in a given time interval depends of course on the defect concentration. If c denotes the KOH doping level, *i.e.*, the concentration of OH^- defects, then on average about $c^{-1/3}$ water molecules are separated by two defects. For instance, with $c = 10^{-3}$ this means that roughly ten jumps are necessary to reach any lattice site from a given defect site. This suggests that for $c \sim 10^{-3}$ or larger scenario (b) is more relevant. It is encouraging that already for scenario (a), the return-to-origin probability is quite sizeable and it can be conceived that the corresponding single-site passage probability is even larger for scenario (b). Quantitative estimates will have to take into account path blocking effects analogous to those discussed in Appendix B. These effects and their averaging over all configurations that are compatible with the Bernal–Fowler rules are dealt with more efficiently *via* appropriate computer simulations which are beyond the scope of the present paper.

The simple arguments presented here suggest that for the current doping levels we should consider the passage of several distinct OH^- defects at a given lattice site rather than loop-related processes. But still, with the probability p of about $\leq 10^{-3}$ that a

given site is visited three times by a defect, a very fast OH^- motion is necessary given the constraint that the six orientations are all reached on a time scale τ_c of milliseconds at $T \approx 70$ K for the KOH doped clathrate or at $T \approx 100$ K for KOH doped ice, see Fig. 2. Hence, at these temperatures the elementary jump of the OH^- defect is expected to take place on a time scale $\tau_e \approx \tau_c p \leq 1$ μs.

C. Defect mobility

A fast hopping motion of ionic defects, *e.g.*, of the hydronium ion, was recently observed *via* quasi-elastic neutron scattering in HCl doped ice I_h.[60] When extrapolated to temperatures near 100 K and consistent with thin film diffusion experiments[61,62] time constants of a few hundred nanoseconds were found.[63] Such values are compatible with the condition just stated for τ_e at the end of Section IV.B. However, it has to be kept in mind that the mobility of the hydroxyl ion is lower than that of the hydronium ion (in nominally pure ice[64] by a factor of 3 at −20 °C and by more than one decade for ammonia doped ice[65,66] at $T = 155$ K). From the cited studies it is not possible to draw firm conclusions concerning the mobility of the OH^- defect in KOH doped ice because different base dopants can generate different combinations of defects when incorporated into the ice lattice: NH_3 creates ionic OH^- species plus Bjerrum D defects, whereas KOH triggers the formation of Bjerrum L defects in addition to OH^- moieties. Furthermore, the potassium ion is believed to occupy an interstitial lattice site[1] whereas ammonia occupies a water lattice position thus raising the possibility that not only the mobility[64] but also the trapping ability of the various Bjerrum defects is quite different and that it will also markedly depend on their concentration. While hydroxide mobility can be strongly impeded by adding small amounts of ammonia to ice,[65,67,68] in ref. 68 it is stated that the OH^- activity is significantly enhanced when the hydroxide ion concentration is sufficiently large. A debated argument in favor of the high mobility in strongly KOH doped ice and KOH doped hydrate is indeed that the phase transition is triggered by the accelerated mobility attained through the dopant.[11,13,69]

Returning to the variation of the dopant it is worthwhile to mention that HCl doping is more effective in speeding up the dynamics in ice I_h and THF clathrate hydrates than doping with NH_3.[70] But doping with KOH is even more effective than doping with HCl: we have measured HCl doped clathrates near 100 K and we find that the dielectric time constants of HCl are 3 orders of magnitude larger than those for KOH doped hydrates.[71] Similar results were also reported for doped ice.[44]

D. Doped ice *versus* doped clathrates

Much of the preceding discussion focused on KOH doped hexagonal ice. However, the simulations presented in Appendix A suggest that the arguments regarding the motional process can be applied also to the doped clathrate hydrates. However, there are also a few differences between the two crystals: when comparing the time constants obtained from dielectric and from NMR spectroscopy, good overall agreement for doped hexagonal ice is found, see Fig. 2, confirming similar observations reported for undoped ice in certain temperature ranges.[31] If a small-angle reorientation is to be associated with these time constants, then the agreement of dielectric and NMR data is expected.[72] Due to the different angular sensitivities of dielectric spectroscopy (order of Legendre polynomial $\ell = 1$) and NMR ($\ell = 2$) the respective time scales τ_ℓ differ only slightly: one has $\tau_2/\tau_1 = 1/3$ for three-dimensional (*i.e.*, isotropic) rotational diffusion, but this ratio can become larger than unity for large jump angles φ.[73] For $\varphi \to 180°$, an angle under which tensorial NMR quantities are invariant, τ_2/τ_1 even diverges. However, in the presence of a distribution of jump angles, τ_2/τ_1 remains finite and for sufficiently broad distributions this ratio approaches unity even for mean jump angles of 180°.[74] This line of arguments is obviously applicable to the ice data. On the other hand, the dielectric time scales and those determined using NMR differ for the clathrate hydrates, a finding which warrants further study.

V. Summary

In this work we performed dielectric and deuteron NMR measurements on THF clathrate hydrates and hexagonal ice, both doped with (sub-) percent amounts of potassium hydroxide. KOH doping accelerates the dynamics in these crystals by up to 10 orders of magnitude with respect to the undoped crystals. From NMR experiments we found that in the clathrate hydrate the degree of speed-up depends on the prior cooling rate. For instance the spin–spin relaxation times exhibit shallow minima near 85 K (fast cooling) or 105 K (slow cooling). 'Shallow' means that the minimal T_2 times are roughly two orders of magnitude longer than expected for an isotropic reorientation process. Hence, in the corresponding temperature ranges the deuteron spectra should exhibit only minor, but significant line shape changes in accord with our experimental findings. From these experiments correlation times are inferred which are not incompatible with those derived from the two-time auto-correlation functions acquired using the stimulated-echo technique. The corresponding measurements were carried out for the KOH doped clathrates from about 100 K down to just above the order–disorder transition taking place near 60 K. Apart from time scales, the evolution time dependence of the two-time correlation functions also yielded information regarding the geometry of the motional process. Based on a comparison with random-walk simulations a jump process among six different sites was identified and the associated effective jump angles turned out to be about $\alpha = 2°$ (or $180° - \alpha$ which cannot be distinguished by NMR experiments). These angles are compatible with the non-linearity of the O–H···O bond. The six orientations of the corresponding deuteron bonds are reached on times scales that are at least 3 decades shorter than those on which large-angle jumps of entire water molecules take place. The newly identified effective small-angle jumps occur only in doped crystals and therefore they are certainly linked to the motion of ionic defects. Our experimental findings for the doped clathrate hydrates are well established and the same trends can be inferred for KOH doped ice. But here the data

base is much less extensive due to enormously long spin-lattice relaxation times of ice which would necessitate unacceptably time consuming experiments.

The microscopic motional processes responsible for our observations were discussed to involve either loop-type motions of single OH^- defects or passages of several defects at a given lattice site. Based on probability arguments partially accounting for the Bernal–Fowler ice rules, the latter scenario was found to be more likely given the relatively large defect concentrations present in the currently studied crystals. A prediction of our considerations is that a fast defect-related transport process should be active in doped ice phases. This expectation was discussed in relation to a fast hopping motion as recently detected *via* quasielastic neutron scattering in ices doped, however, with different defects. Thus, such experiments should be carried out also for suitably doped clathrate hydrates.

Appendix A: numerical simulations of cone motions

The simulation of proton transfer processes and of small-angle motions were set up as follows. As sketched in the upper inset of Fig. 11 we define three orientations (marked 1 in that figure) of the OH bonds or, more precisely, of the largest principal axis of the corresponding EFG tensors which we assume to be axially symmetric ($\eta = 0$). Jumps among these positions can thus be viewed as a motion on the cone mantle and we take its opening angle to be 2α. Three further orientations (marked 2) are obtained by taking into account the mirror plane which locally exists between two adjacent oxygen atoms and which is sketched in the upper inset of Fig. 11. Due to the symmetry of the second Legendre polynomial, implied by eqn (1) with $\eta = 0$, a proton transfer (a jump across the mirror plane) in terms of frequency change is equivalent to a jump across the dotted mirror plane (cutting through the oxygen atom shown in that figure). In other words, $\omega_{Q,0} = \frac{1}{2}\delta(3\cos^2\theta - 1)$ is the same for the positions marked 2 and 2′.[75] It is important to realize that while the jump angles φ among the OH orientations spanning the cone are small, those angles corresponding to a proton transfer process (jump to the adjacent cone) are close to 180°. Nevertheless, since $\omega_{Q,0}(\theta) = \omega_{Q,0}(\pi - \theta)$ the frequency changes are small in both situations. We restrict the discussion here to random jumps, *i.e.*, the transition rates κ_{ij} between any two orientations i and j are taken to be equal. But other conditions (*e.g.*, diffusion-type processes with $\kappa_{ij} \neq 0$ only for $|i - j| = 1$) are also simple to implement.

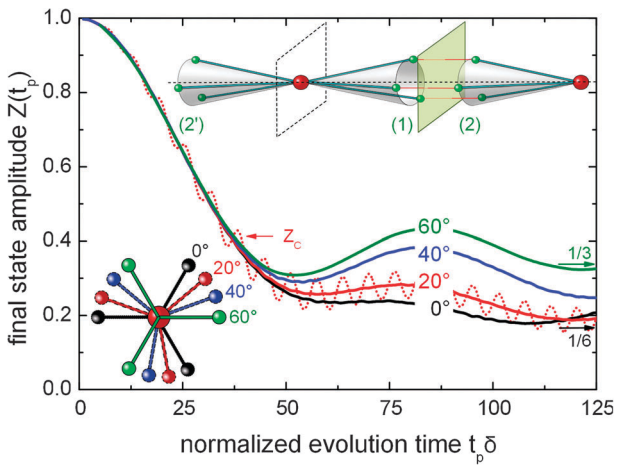

Fig. 11 Evolution time dependent final state amplitudes for the twisted double cone model for a cone opening angle of $2\alpha = 4°$. There are three equally spaced sites on each cone so that $N = 6$. The twist angles are $\gamma = 0$, 20, 40, and 60°. The result for $\gamma = 0°$ is identical to that in Fig. 7(b). For $\gamma = 20°$ the wiggling final-state amplitude, Z_c (broken curve), is obtained by analyzing F_2^c rather than F_2^+. The upper inset depicts the local jump geometry [*cf.* Fig. 8(b)] as used for the computer simulations. The planes highlight local mirror symmetries that exist only for $\gamma = 0$. The dotted line emphasizes the local three-fold axis. The numbers are used to label the groups of proton positions as explained in the text. The lower inset is meant to visualize a view along the three-fold axis from which the twist angles γ is most easily inferred. The arrows indicate $Z(t_p \to \infty)$ yielding 1/6 for $\gamma \neq 60°$ and 1/3 otherwise.

Then, a random orientation for the external magnetic field was chosen and a trajectory $\omega_Q(t)$ was generated from which $f_2^c(t_p, t_m) \equiv \cos[\omega_Q(0)t_p]\cos[\omega_Q(t_m)t_p]$, *cf.* eqn (2), and its sin–sin variant $f_2^s(t_p, t_m)$ were calculated. In order to achieve global isotropy (*i.e.*, to perform a powder average) this procedure was repeated typically 10^5 times while for the start of each trajectory a random orientation was chosen for the angle enclosed by the cone axis and the external magnetic field. Then, the powder averaged functions $F_2^c(t_p, t_m) = \langle f_2^c(t_p, t_m)\rangle \equiv F_2(t_p, t_m)$ and likewise $F_2^s(t_p, t_m)$ were calculated, fitted using eqn (3), and used to obtain, *e.g.*, $Z^+(t_p) = \frac{1}{2}[Z^c(t_p) + Z^s(t_p)]$ as well as other parameters shown in Fig. 7.[76]

The local structure of the cubic structure II clathrate hydrates can be considered as a distorted variant of the local structure of hexagonal ice which we have dealt with in this Appendix so far. Viewing along the C_3 symmetry axis of the structural element shown in the upper inset of Fig. 11, always two of the projections of the $N = 6$ magnetically inequivalent OH bonds superpose. This is sketched in the lower inset of Fig. 11 by the lines labeled $\gamma = 0°$. We mimic the distorted local symmetry in the clathrate hydrates by assuming that two adjacent cones are twisted about an angle γ with respect to each other. In the lower inset of Fig. 11 additional examples are provided for twist angles of $\gamma = 20°$, 40°, and 60°. The latter case ($\gamma = 60°$) is a degenerate one because two orientations each are then related *via* an inversion symmetry so that only three magnetically inequivalent OH bonds exist. In Fig. 11 simulations of Z are shown for $\gamma = 0°$, 20°, 40°, and 60°. A detailed comparison (not shown) with the experimental results obtained for $T = 75.1$ and 72.6 K reveals that effective twist angles $\gamma > 20°$ are inadequate, in harmony with results from diffraction experiments.[10]

To explore the cone-type simulations further, we generalized our model ($\gamma = 0°$, $N/2$ equally spaced sites on each cone) to take into account other than 6 orientations. In Fig. 12 we show results $Z(t_p)$ (i) for $N = 2\ldots1000$ and a cone opening half angle $\alpha = 2°$ (solid lines) and (ii) for $N = 100$ and $\alpha = 1°$, 3°, 4°, and 10° (dashed lines). It is clear that $Z(t_p) = 1/N$ is asymptotically approached. Furthermore, for $N \to \infty$ we find $Z \propto t_p^{-0.82}$.

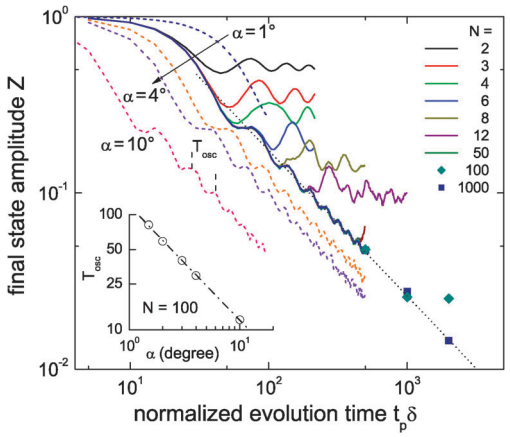

Fig. 12 Double logarithmic representation of the final state amplitude as a function of the evolution time for random jumps among N equally spaced sites on a cone mantle with a half opening angle of α. The solid lines are for $\alpha = 2^\circ$, the dashed ones correspond to $\alpha = 1^\circ$, 4°, and 10° as indicated and $N = 100$. The definition of the N-specific oscillation period (which is better recognized as such at a linear ordinate scale, not shown) is illustrated. For $N = 100$ (diamonds) and $N = 1000$ (squares) and large $t_p\delta$ the (time-consuming) simulations were carried out only for a few t_p. The dotted line represents $Z \propto t_p^{-1}$. The inset illustrates the dependence of the oscillation period on the cone opening angle for $N = 100$. The circles represent the oscillation periods T_{osc} determined from simulations. The solid line reflects $T_{osc} = N/\alpha$ with α in degree.

We analyzed these $Z(t_p)$ patterns in more detail. For instance, we determined the smallest evolution time t_p^x at which $Z(t_p)$ crosses $1/N$ and found $t_p^x\delta_Q \propto \alpha^{-1}$ (not shown). We also evaluated the oscillation period T_{osc} that characterizes the undulations seen in $Z(t_p)$. The inset of Fig. 12 shows that we found $T_{osc} \propto \alpha^{-1}$ for $N = 100$ and α ranging from 1° to 10°.

Appendix B: probability for the return of an OH^- defect to its initial site

Let us consider a ring that is one of the six traversable ones mentioned in Section IV.B, then what is the probability that its H-bond configuration allows for a complete roundtrip of an OH^- defect? If we consider a path *via* a lattice site conductive for an OH^- defect (which has to involve a proton at its entrance and a lone-pair at its exit), then two of the hydrogen bonds are already in the right orientation. This is symbolized by the green arrows in Fig. 13(b). We then have to inquire about the conditional probability that the third bond along the ring sketched in Fig. 13(b) is in the right orientation, given that the second bond is. There are six general orientations for a water molecule on a given lattice site, see Fig. 13(a). In the representation of Fig. 13(b) the Bernal–Fowler rules require that two arrows point towards each oxygen atom and two arrows point away from it. This leaves one with only two out of six possible orientations of the water molecule [sketched in first and second position in Fig. 13(a)]. Analogous arguments hold for the four remaining bonds that are symbolized by the red arrows in Fig. 13(b). The conditional probability for each of them being in the right orientation, given that their neighbor is in the right position, is 2/3.

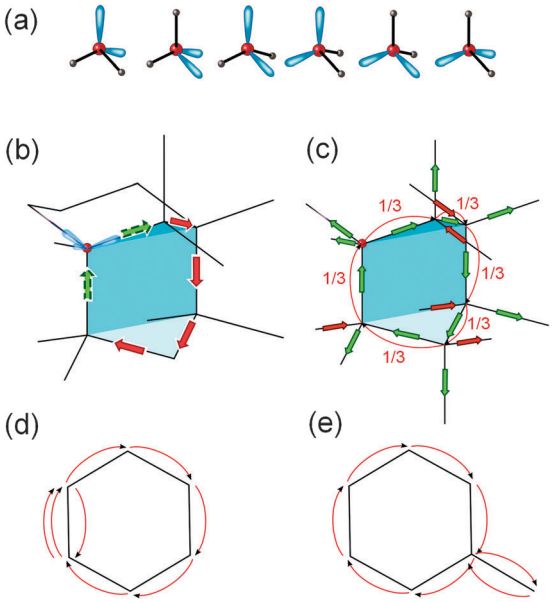

Fig. 13 (a) The six possible orientations of a water molecule on a suitably chosen lattice site. (b) In a conductive 6-ring a strictly alternating proton/lone-pair sequence along the path is required, here symbolized by the arrows. With two bonds (symbolized by the green broken arrows) already defined by a properly oriented water molecule, the probability that the loop is traversable is almost 20%, *cf.* eqn (6). (c) Illustration of the return-to-origin probability $P_6^{RTO} \approx 0.14\%$ for a 6-step loop, *cf.* eqn (7). Frames (d) and (e) provide two examples for topologically different 8-step loops in a two-dimensional representation. Each vertex is connected to two further bonds with one of them always being accessible.

Hence, we conclude that if a ring is one of the six ones that can be entered from the site marked in Fig. 9, then with a probability

$$P = (2/3)^4 = 0.1975, \quad (6)$$

it will be conductive for OH^- ions. This can alternatively be expressed by stating that every OH^- ion on average is a member of about one conductive 6-ring (more precisely of $6P = 1.185$ of such rings).

This a relatively large number, but even more important is the return-to-origin (RTO) probability P^{RTO}. So far we considered that a roundtrip of an OH^- group can be completed in $s = 6$ steps and a corresponding 6-step loop is sketched in Fig. 13(c). Of course, larger loops with even numbers of steps can also be found. Furthermore, for large enough loops there will be a large multiplicity (quantified by the number l) of distinguishable loops. But for the completion of a 6-step loop only one ($l = 1$) distinguishable sequence of steps exists. Since at every vertex the OH^- group can move along one out of three ways, the probability for it to go the "right" one (the one which leads to fastest closure of the 6-step loop) is $\frac{1}{3}$. Hence, the overall RTO probability

$$P_s^{RTO} = l\left(\frac{1}{3}\right)^s, \quad (7)$$

is 0.00137. The return to the origin in this case obviously requires $s = 6$ time steps.

Of course larger loops (always with s even) can easily be constructed. Fig. 13(d) and (e) depict examples of different 8-step loops. Here the multiplicity is $l = 12$ since the sketched back-and-forth jumps can happen along each of the six edges of the ring [*cf.* Fig. 13(d)] or emanate from each of its six vertices [*cf.* Fig. 13(e)]. Hence $P_8^{\mathrm{RTO}} = 12(\frac{1}{3})^8 = 0.00183$, but the time for the return to the origin is 8/6 times longer than for the 6-step loop. For $s = 10$ one finds $P_{10}^{\mathrm{RTO}} = 0.00244$ (not illustrated).

A general analytical scheme for the construction and evaluation of the graphs corresponding to more complex loops is not available to us. For the mathematical treatment of this problem it will probably be useful to take into account the schemes developed for an accurate determination of the configurational entropy of disordered ice phases,[77–79] that go beyond the simple arguments leading to the Pauling entropy.

Acknowledgements

We thank Kay Saalwächter for stimulating discussions regarding the Anderson–Weiss theory. Funding by the Deutsche Forschungsgemeinschaft *via* Grant No. BO1301/7-2 is gratefully acknowledged.

References

1 V. F. Petrenko and R. W. Whitworth, *Physics of Ice*, University Press, Oxford, 1999.
2 C. G. Salzmann, P. G. Radaelli, A. Hallbrucker, E. Mayer and J. L. Finney, *Science*, 2006, **311**, 1758; C. G. Salzmann, P. G. Radaelli, E. Mayer and J. L. Finney, *Phys. Rev. Lett.*, 2009, **103**, 105701.
3 M. Bauer, K. Winkel, D. M. Toebbens, E. Mayer and T. Loerting, *J. Chem. Phys.*, 2009, **131**, 224514.
4 H. Fukazawa, S. Mae, S. Ikeda and O. Watanabe, *Chem. Phys. Lett.*, 1998, **294**, 554; A. D. Fortes, I. G. Wood, D. Grigoriev, M. Alfredsson, S. Kipfstuhl, K. S. Knight and R. I. Smith, *J. Chem. Phys.*, 2004, **120**, 11355.
5 H. Fukazawa, A. Hoshikawa, B. C. Chakoumakos and J. A. Fernandez-Baca, *Nucl. Instrum. Methods Phys. Res., Sect. A*, 2009, **600**, 279.
6 S. Kawada, *J. Phys. Soc. Jpn.*, 1972, **32**, 1442.
7 C. G. Salzmann, P. G. Radaelli, B. Slater and J. L. Finney, *Phys. Chem. Chem. Phys.*, 2011, **13**, 18468.
8 O. Yamamuro, M. Oguni, T. Matsuo and H. Suga, *J. Phys. Chem. Solids*, 1988, **49**, 425.
9 O. Yamamuro, T. Matsuo and H. Suga, *J. Inclusion Phenom.*, 1990, **8**, 33.
10 R. K. McMullan and A. Kvick, *Acta Crystallogr., Sect. B: Struct. Sci*, 1990, **46**, 390.
11 H. Suga, *Proc. Jpn. Acad., Ser. B*, 2005, **81**, 349.
12 See Chapter 5.4.3.4 of ref. 1 and references cited therein.
13 H. Nelson, A. Nowaczyk, C. Gainaru, S. Schildmann, B. Geil and R. Böhmer, *Phys. Rev. B: Condens. Matter Mater. Phys.*, 2010, **81**, 224206.
14 Y. Tajima, T. Matsuo and H. Suga, *Nature*, 1982, **299**, 810.
15 Y. Tajima, T. Matsuo and H. Suga, *J. Phys. Chem. Solids*, 1984, **45**, 1135.
16 S. Alavi, R. Susilo and J. A. Ripmeester, *J. Chem. Phys.*, 2009, **130**, 174501.
17 V. Buch, J. P. Devlin, I. A. Monreal, B. Jagoda-Cwiklik, N. Uras-Aytemiz and L. Cwiklik, *Phys. Chem. Chem. Phys.*, 2009, **11**, 10245.
18 The low temperature phase is orthorhombic, see O. Yamamuro, T. Matsuo, H. Suga, W. I. F. David, M. Ibberson and A. J. Leadbetter, *Physica*, 1995, **213 and 214**, 405.
19 See ref. 13 and references cited therein.
20 J. Baia, C. A. Angell and X. C. Zeng, *Proc. Natl. Acad. Sci. U. S. A*, 2010, **107**, 5718. These authors point out that so far only Ge and Si based guest-free clathrates have been found experimentally.
21 L. C. Jacobson, W. Hujo and V. Molinero, *J. Phys. Chem. B*, 2009, **113**, 10298.
22 J. S. Tse, M. Desando, J. A. Ripmeester and Y. P. Handa, *J. Am. Chem. Soc.*, 1993, **115**, 281; G. A. Tribello, B. Slater, M. A. Zwijnenburg and R. G. Bell, *Phys. Chem. Chem. Phys.*, 2010, **12**, 8597.
23 S. Klotz, L. E. Bove, T. Strässle, T. C. Hansen and A. M. Saitta, *Nat. Mater.*, 2009, **8**, 405.
24 Y. Yoshimura, *High Pressure Res.*, 2009, **29**, 542.
25 G. P. Johari, *J. Chem. Phys.*, 1998, **109**, 9543.
26 C. G. Salzmann, A. Hallbrucker, J. L. Finney and E. Mayer, *Phys. Chem. Chem. Phys.*, 2006, **8**, 3088.
27 S. J. Singer and C. Knight, *Adv. Chem. Phys.*, 2012, **147**, 1; T. Bartels-Rausch, V. Bergeron, J. H. E. Cartwright, R. Escribano, J. L. Finney, H. Grothe, P. J. Gutierrez, J. Haapala, W. F. Kuhs, J. B. C. Pettersson, S. D. Price, C. I. Sainz-Diaz, D. J. Stokes, G. Strazzulla, E. S. Thomson, H. Trinks and N. Uras-Aytemiz, *Rev. Mod. Phys.*, 2012, **84**, 885.
28 M. de Koning, A. Antonelli, A. J. R. da Silva and A. Fazzio, *Phys. Rev. Lett.*, 2006, **97**, 155501.
29 F. Fujara, S. Wefing and W. F. Kuhs, *J. Chem. Phys.*, 1988, **88**, 6801.
30 M. Bach-Vergés, S. J. Kitchin, K. D. M. Harris, M. Zugic and C. A. Koh, *J. Phys. Chem. B*, 2001, **105**, 2699.
31 B. Geil, T. M. Kirschgen and F. Fujara, *Phys. Rev. B: Condens. Matter Mater. Phys.*, 2005, **72**, 014304.
32 T. M. Kirschgen, M. D. Zeidler, B. Geil and F. Fujara, *Phys. Chem. Chem. Phys.*, 2003, **5**, 5243.
33 A. Nowaczyk, S. Schildmann, B. Geil and R. Böhmer, *Phys. Rev. B: Condens. Matter Mater. Phys.*, 2009, **80**, 144303.
34 W. R. Groves and C. H. Pennington, *Chem. Phys.*, 2005, **315**, 1.
35 Y. Ba, J. A. Ripmeester and C. I. Ratcliffe, *Can. J. Chem.*, 2011, **89**, 1055.
36 A. J. Leadbetter, R. C. Ward, J. Q. W. Clark, P. A. Tucker, T. Matsuo and H. Suga, *J. Chem. Phys.*, 1985, **82**, 424.
37 M. Oguro, *J. Phys. Chem. Solids*, 2001, **62**, 897.
38 At these concentrations the mole fraction, $x = n_{\mathrm{KOH}}/(n_{\mathrm{KOH}} + n_{\mathrm{D2O}})$, with $n = m/M_{\mathrm{mol}}$ denoting the number of molecules and M_{mol} the molar mass, is indistinguishable from the

molar ratio n_{KOH}/n_{D2O}. The nominal KOH concentration in mol l^{-1} can be calculated by $x \times 1000$ g/18 g.
39 An even faster T_1 contribution than shown in Fig. 1 was observed for KOH doped hexagonal ice which, however, is not in the focus of the present work, see S. Schildmann, A. Schöler, A. Nowaczyk, B. Geil and R. Böhmer, *Appl. Magn. Reson.*, 2013, **44**, 203.
40 S. K. Garg, D. W. Davidson and J. A. Ripmeester, *J. Magn. Reson.*, 1974, **15**, 295.
41 D. Davidson, S. K. Garg and J. A. Ripmeester, *J. Magn. Reson.*, 1978, **31**, 199.
42 R. Howe and R. W. Whitworth, *J. Phys. Chem. Solids*, 1989, **50**, 963, report on the electrical conductivity of KOH doped ice.
43 M. Oguro and R. W. Whitworth, *J. Phys. Chem. Solids*, 1991, **52**, 401.
44 S. Kawada, J. G. Ru and A. Mituru, *J. Phys. Chem. B*, 1997, **101**, 6223.
45 S. Kawada and R. Tutiya, *J. Phys. Chem. Solids*, 1997, **58**, 115.
46 R. Böhmer, G. Diezemann, G. Hinze and E. Rössler, *Prog. Nucl. Magn. Reson. Spectrosc.*, 2001, **39**, 191.
47 G. Diezemann and H. Sillescu, *J. Chem. Phys.*, 1995, **103**, 6385.
48 J. R. Klauder and P. W. Anderson, *Phys. Rev.*, 1962, **125**, 912.
49 D. E. Woessner, *Concepts Magn. Reson.*, 1996, **8**, 397.
50 R. Kimmich, *Tomography, Diffusion, Relaxometry*, Springer, Berlin, 1997, pp. 120 ff.
51 The case of a free induction signal arising from a correlation function decaying to zero (corresponding to isotropic motion) was explicitly dealt with in ref. 49, see in particular p. 421ff where results for solid-echo refocusing are also presented. Furthermore, echoes in the presence of isotropic motions are treated in ref. 48.
52 K. Saalwächter, *Prog. Nucl. Magn. Reson. Spectrosc.*, 2007, **51**, 1 discusses anisotropic models in detail.
53 G. Fleischer and F. Fujara, in *NMR - Basic Principles and Progress*, ed. P. Diehl, E. Fluck, H. Günther, P. Kosfeld and J. Seelig, Springer, Berlin, 1994, vol. 30, p. 160, see in particular their Fig. 5.
54 J.-L. Kuo, M. L. Klein and W. F. Kuhs, *J. Chem. Phys.*, 2005, **123**, 134505 point out that the proton disorder in ice I_h hampers a precise experimental determination of the HOH bending angle and from a theoretical study they find $106.3^\circ \pm 0.4^\circ$.
55 Based on density functional calculations G. S. Fanourgakis and S. S. Xantheas, *J. Chem. Phys.*, 2006, **124**, 174504 report bending angles of $108.1^\circ \ldots 108.4^\circ$ for ice I_h.
56 G. Hinze, *Phys. Rev. E*, 1998, **57**, 2010.
57 M. Vogel and E. Rössler, *J. Magn. Reson.*, 2000, **147**, 43.
58 B. Geil, G. Diezemann and R. Böhmer, *J. Chem. Phys.*, 2008, **128**, 114506.
59 The calculated lines in Fig. 7 are left-shifted by 4 μs to account for the finite width of the radio-frequency pulses.
60 I. Presiado, J. Lal, E. Mamontov, A. I. Kolesnikov and D. Huppert, *J. Phys. Chem. C*, 2011, **115**, 10245.
61 A. Uritski, I. Presiado and D. Huppert, *J. Phys. Chem. C*, 2008, **112**, 11991.
62 A. Uritski, I. Presiado, Y. Erez, R. Gepshtein and D. Huppert, *J. Phys. Chem. C*, 2009, **113**, 10285.
63 In principle such a time scale should be resolvable using spin-lattice relaxation experiments. However, we found no signatures of a process taking place on a time scale of nanoseconds around temperatures of 100 K. Given that for each OH^- proton there are about 2000 H_2O protons, our NMR experiments may simply not be sensitive enough.
64 See Table 6.4 of ref. 1.
65 W. B. Collier, G. Ritzhaupt and J. P. Devlin, *J. Phys. Chem.*, 1984, **88**, 363.
66 J. P. Devlin, *Phys. Chem. Chem. Phys.*, 2011, **13**, 19707.
67 E. S. Moon, Y. Kim, S. Shin and H. Kang, *Phys. Rev. Lett.*, 2012, **108**, 226103.
68 L. Cwiklik, J. P. Devlin and V. Buch, *J. Phys. Chem. A*, 2009, **113**, 7482.
69 C. Knight and S. J. Singer, in: *Physics and Chemistry of Ice*, ed. W. F. Kuhs, Royal Society of Chemistry, London, 2007, pp. 339–346.
70 D. Arias, L. Levi and L. Lubart, *Trans. Faraday Soc.*, 1966, **62**, 1955; M. Hubmann, *Z. Phys. B: Condens. Matter Quanta*, 1979, **32**, 127; H. Didzoleit, C. Gainaru, B. Geil and R. Böhmer (unpublished).
71 H. Nelson *et al.* (unpublished).
72 Regarding the magnitude of the jump angle in liquid water it was stated that ''the jury is still out'', see R. Ludwig, *Angew. Chem., Int. Ed.*, 2006, **45**, 3402; R. Ludwig, *ChemPhysChem*, 2007, **8**, 44.
73 J. E. Anderson, *Faraday Symp. Chem. Soc.*, 1972, **6**, 82.
74 J. E. Anderson, *Faraday Symp. Chem. Soc.*, 1972, **6**, 91.
75 For the twist angle $\gamma = 0$, defined in Appendix A, the situation of N mirrored sites on 2 cones is equivalent to $2N$ equally spaced sites on a single cone.
76 The advantage of using co-added F_2-functions or parameters derived thereof is that the t_p-dependent wiggles, exemplified in Fig. 11 for the final-state amplitude Z_c, are often smeared out in real experiments and hence allow for a better comparison with simulations.
77 G. T. Hollins, *Proc. Phys. Soc., London*, 1964, **84**, 1001.
78 T. V. Lokotosh and O. M. Gorun, *J. Low Temp. Phys.*, 2003, **29**, 230.
79 L. G. MacDowell, E. Sanz, C. Vega and J. L. F. Abascal, *J. Chem. Phys.*, 2004, **121**, 10145.